Available online at www.sciencedirect.com
SCIENCE DIRECT®
Continental Shelf Research 24 (2004) 483–507
CONTINENTAL SHELF RESEARCH
www.elsevier.com/locate/csr

Modelling the morphodynamics of a tidal shelf sea

J. van der Molen*, J. Gerrits, H.E. de Swart

Institute for Marine and Atmospheric Research Utrecht (IMAU), Utrecht University, Princetonplein 5, Utrecht 3584 CC, The Netherlands

Received 24 April 2003; received in revised form 29 October 2003; accepted 4 December 2003

Abstract

Results are presented of numerical simulations of the basin-scale morphodynamics of an idealised, semi-enclosed, energetic tidal shelf sea. The basin dimensions and tidal characteristics resemble those of the Southern Bight of the North Sea. The simulations were carried out using a finite-difference model of bed-level change, designed for use with an existing numerical hydrodynamical model. A 'bottom–up' approach was chosen, which allows investigation of basic physical effects. A bed-load sediment-transport formulation was used, assuming uniform grain size. The computations focus on the basin-scale evolution of the seabed (hundreds of kilometres), span several tens of thousands of years, and represent various scenarios of sea-level change. Morphological features with length scales of tidal sandbanks and smaller were not included. The results show that the basin will export sediment and deepen. Also, it will expand by the accumulation of the eroded sediment in the deeper waters to the north. The deepening causes reduction of the flow velocities and the net sediment transport, resulting in decreasing rates of morphodynamic evolution. The resulting large-scale seabed topography partly resembles the current bathymetry of the Southern Bight of the North Sea. The topography is mainly the result of sediment redistribution along the longitudinal axis of the basin, caused by asymmetry in the velocity field of the amphidromic system. The feedback of the developing bed levels to the water motion is dominated by the increase in water depth, and much less by the seabed topography. Externally prescribed changes in sea level change the wavelengths of the tide and the seabed pattern; they also change the speed of the morphodynamical evolution.

Keywords: Morphodynamic equilibrium; Tides; Sediment transport; Model; Taylor's problem; North Sea

1. Introduction

1.1. Motivation

Shelf seas like the North Sea are characterised by tidal currents strong enough to erode and transport sediment. Field observations show a clear pattern of sand fluxes in the North Sea (Johnson et al., 1982). Spatial divergence of these fluxes changes the morphology, resulting in bed

*Corresponding author. Present address: Faculty of Science and Engineering, Dalton Research Institute, Manchester Metropolitan University, John Dalton Building, Chester Street, Manchester M1 5GD, UK. Tel.: +44-161-247-3589; fax: +44-161-247-1483.

E-mail address: j.vandermolen@mmu.ac.uk, j.vandermolen@phys.uu.nl (J. van der Molen).

0278-4343/$ - see front matter © 2004 Elsevier Ltd. All rights reserved.
doi:10.1016/j.csr.2003.12.001

forms and basin-scale bathymetric evolution. Current-generated bed forms are tidal sandbanks with length scales of several kilometres (e.g., Dyer and Huntley, 1999) and sand waves with length scales of several hundreds of metres (e.g., Huntley et al., 1994). The basin-scale morphodynamic evolution takes thousands of years. It is influenced strongly by changes in coast-line geometry and water depth caused by variations in mean sea level (e.g., Lambeck, 1995).

This paper focuses on the basin-scale morphodynamic evolution. Models based on equations for depth-averaged tidal flow and sand transport reproduce the observed sand fluxes in the Southern Bight of the North Sea quite well (Gerritsen and Berentsen, 1998; Van der Molen and De Swart, 2001). Their simulations suggested feedback between tides and seabed topography on a scale of hundreds of kilometres. This feedback might lead to morphodynamic equilibrium. Then, tides and seabed topography are adjusted such that the divergence of the tide-averaged sediment transports is zero. If such interaction exists and can be understood, important information can be obtained about the evolution of semi-enclosed shelf seas. Morphodynamic evolution of shelf seas may be important for the evolution of the adjacent coasts, because the sea can be an active source or sink of sediment.

Van der Molen and De Swart (2001) computed the pattern of sediment transport and bed-level change in the Southern Bight for both the realistic bathymetry and a flat bottom at average depth. Larger sediment-transport rates were obtained for the case of a flat bottom, while the main patterns of bed-level change were similar. The patterns indicated a trend to develop important parts of the present bathymetry in a period of time equivalent to the Holocene (10,000 years). During the Holocene the North Sea was flooded after the last glaciation. The smaller transport rates for the realistic bathymetry suggest a trend towards morphodynamic equilibrium.

Feedback between tides and sea-bed topography and morphodynamic equilibrium conditions have been described for tidal basins of lengths of tens of kilometres (Schuttelaars and De Swart, 2000; Van Leeuwen and De Swart, 2001; Lanzoni and Seminara, 2002). The basic physical mechanisms are also present in semi-enclosed tidal shelf seas like the Southern Bight of the North Sea. Thus feedback can be expected, and possibly also morphodynamic equilibria.

This paper tests the hypothesis that morphodynamic equilibria exist for energetic tidal shelf seas on a spatial scale of hundreds of kilometres. The morphodynamical evolution and the physical mechanisms responsible are analysed. Also, the role of changes in mean sea level on the morphodynamical evolution is studied. The specific objective is a first investigation of the main, large-scale interactions between tides and bathymetry in a shelf sea in an idealised context. As such, details in the model results can be expected to differ from situations in the real world. To illustrate the strengths and weaknesses of the results, comparison is made with the Southern Bight of the North Sea, which is well studied, and can be regarded as a prototype semi-enclosed tidal shelf sea. This is a bottom–up approach, which allows for refinements and additions later on.

1.2. Method

A process-based morphodynamical model was developed for this study. The model contains only the most important physical mechanisms governing tidal propagation and sediment transport in a shelf sea. In the following, the main approximations in the model are motivated.

The waters of the Southern Bight of the North Sea are well mixed (e.g., Otto et al., 1990). Thus, stratification does not occur, and the water motion can be simulated with a depth-averaged model. For this study, the existing HAMburg Shelf Ocean Model (HAMSOM) (Backhaus, 1983, 1985) was used to compute the hydrodynamics. The HAMSOM model solves the shallow-water equations with a finite-difference method. It uses the Arakawa-C grid (Arakawa and Lamb, 1977). This grid simplifies the design of a morphodynamical code, because depths are defined in the cell centres. More details about HAMSOM are presented in Section 2.2.

The present model does not account for the potentially important effect of veering of the flow direction in the vertical caused by earth rotation.

As most sand is transported very close to the bottom, traditional three-dimensional (3D) models would require a very high vertical resolution to sufficiently resolve the bottom-boundary layer, and would thus require extensive computing time. A promising first effort has been made to develop a fast method to remedy this problem (Shapiro et al., 2004), but this method still has to be adapted for tidal situations.

In reality, wind-induced currents, wind waves, and density-driven currents contribute to the long-term net sediment transport in shelf seas, and hence to the morphodynamical evolution. In our prototype example of the Southern Bight of the North Sea, density-driven currents are only important in the region of fresh-water influence of the river Rhine along the Dutch coast. There is an estuarine-type of density-driven circulation that generates onshore currents with a yearly average of about 3 cm/s near the bottom in a zone with a width of about 20 km (De Ruijter et al., 1992). Storms can induce depth-average surge currents of up to 1 m/s (Flather, 1987). Time-averaged atmospherically induced depth-averaged residual currents are about one-third of their tide-induced counterparts, and have the same direction (Prandle, 1978). During storms, wind waves can induce substantial near-bottom orbital velocities at depths of several tens of metres (Otto et al., 1990). Earlier simulations with a numerical model of hydrodynamics and sediment transport using a realistic geometry (Van der Molen, 2002) have shown that (i) wind waves enhance the tide-induced sediment transport in the Southern Bight of the North Sea with up to a factor of 2 in the north, (ii) wind-induced currents only contribute significantly to the sediment transport in the presence of waves, (iii) moderate storms from the southwest (wind speeds of about 7 m/s) give the largest contribution to the long-term net sand transport, (iv) sand transport by tides is larger than that by storms in most of the Southern Bight, except in the northeast and at the bed-load parting. These results compared well with observations.

The idealised model geometry was inspired on Taylor's problem (Taylor, 1920). Taylor's problem concerns linear tidal dynamics in a frictionless, semi-enclosed rectangular shelf sea of constant depth with the dimensions of the North Sea. Taylor's problem has also been used to investigate the tidal hydrodynamics of the southern Yellow Sea (Zheng et al., 1991). Here, the basin dimensions resemble the smaller Southern Bight of the North Sea (Section 3.2), while the HAMSOM model accounts for non-linearity and friction. The idealised geometry captures the main physics of the tidal system, but eliminates the effects of coastline geometry, which would cause large local gradients in the sand transport. Such gradients would obscure the large-scale trends and would soon cause emergence of the bed in certain grid cells, while the model cannot simulate flooding and drying. Because the contribution of the spring-neap cycle to the sediment transport averages to zero on a monthly time scale (Van de Kreeke and Robaczewska, 1993), the northern open model boundary was forced with M_2 tidal amplitudes only.

As we focus on internal, large-scale tidal shelf-sea processes, near-shore processes and sediment exchange (rivers, estuaries, beaches) are excluded. In reality, coasts provide local sources and sinks of sediment, which may interact with shelf-sea evolution.

The seabed of the Southern Bight of the North Sea consist mostly of fine to medium sand. The grain size becomes finer from south to north (combine the maps of Cameron et al., 1984a; Harrison et al., 1987; Balson et al., 1991). Very fine material (silt, mud and organic matter) is suspended in the water column, but rarely settles longer than a few hours (Williams et al., 1998). Thus, only sand participates in morphodynamical evolution, and finer material is ignored. For simplicity, a single grain size is assumed here.

For sand with grain sizes typical for the Southern Bight of the North Sea (250 μm), fall velocities are such that sand grains will settle within a distance comparable to the resolution of the model on the tidal time scale. Moreover, the model grid size is of the same order of magnitude as the tidal excursion length. As a result, solving the advection–diffusion equations for sediment transport will not yield more information than a much more simple transport formulation. Suspended and bed-load sand-transport rates in tidal conditions are of comparable magnitude in the Southern Bight of

the North Sea (Van der Molen and De Swart, 2001). Moreover, the transport patterns are similar. Thus, the main trends of morphodynamical evolution can be studied by considering only bed-load transport of sand. A local transport formulation is used (Bailard, 1981), see also Section 2.3. Depth-averaged flow velocities are large in the Southern Bight of the North Sea (typically >0.7 m/s). Thus, a threshold velocity for sediment motion is not included. Because of these simplifications analytical techniques can be used to interpret the results.

Unlimited availability of sand of a single grain size was assumed. In reality, sediment consists of a continuum of grain sizes, and their distribution varies from place to place (Cameron et al., 1984a; Harrison et al., 1987; Balson et al., 1991). Moreover, sand may not be available in unlimited amounts, thus reducing the maximum local transport rate. Grains of different sizes can travel with different speeds, over different distances or even in different directions (e.g., Johnson et al., 1982). These processes are influenced by the threshold of motion. Most of these grain-related processes result in sorting of the sediment, as is indeed evident from the grain-size distribution in the North Sea. Such sorting might result in spatially dependent rates of morphodynamical evolution. Thus, these properties of sand grains will influence the development of a shelf sea. It is not expected, however, that grain-related properties would dominate the qualitative model behaviour as presented here.

As a first approximation, a friction law independent of time and space is used for both the hydrodynamic model and the sediment-transport formulation. In reality, the magnitude of bottom friction may vary in a complicated manner as the hydrodynamics interact with bed forms of scales ranging from ripples (several cm) to sand waves (hundreds of m) and sand banks (several km). Indeed, sand waves have been shown to exert drag on currents in the North Sea (Huntley et al., 1994). Ideally, such bed forms and their drag should be included dynamically in the solution of the morphodynamical model. They are too small, however, to be resolved and generated by the present model. In addition, 3D processes play a role in their formation (Hulscher et al., 1993). Alternatively, parameterisations might be used to predict the full range of possible marine bed form dimensions from sediment characteristics and hydrodynamical conditions. Reliable, accurate full-range parameterisations do not exist to date, however. Dynamically adjusted friction may be important for the morphodynamical evolution of shelf seas, but it will not influence the main trends as presented here.

The bed-level evolution was computed using the Lax–Wendroff method (Lax and Wendroff, 1960), see also Section 2.4. This numerical technique has been used successfully in a variety of morphodynamical models (e.g., Nairn and Southgate, 1993; Ranasinghe et al., 1999; Cayocca, 2001). The Lax–Wendroff method is a finite-difference technique that is second-order accurate in both space and time, and is largely free of numerical diffusion.

The morphodynamical time scale of the model is longer than in reality, because suspended load transport is excluded (factor of about 2), and because storms are excluded (factor of about 2). In the realistic geometry of the Southern Bight of the North Sea, these factors are space dependent because of the average distribution of wave height, which is smallest in the southwest, and largest (exceeding 2) in the northeast. Note, however, that the Bailard formulation as used here overestimates the sediment transport magnitude (a factor 1–5).

Results for various sea-level scenarios are presented (Section 3), starting with stationary sea levels at various elevations. These model experiments identify the main trends in basin evolution, and give a first impression of the influence of sea level on the model solution. Subsequently, two different rates of steady sea-level rise were applied to investigate the dynamic response of the system to external forcing. Finally, the response to sinusoidal sea-level variation was investigated. This model experiment illustrates the effects of a time-varying rising and falling sea level.

2. Model description

2.1. Model structure

The morphodynamical model consists of a feedback loop (see Fig. 1). The hydrodynamics

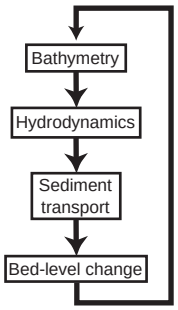

Fig. 1. Morphodynamic feedback loop.

are simulated for a given bathymetry, and yield velocities from which sediment-transport rates are calculated. Next, bed-level change is computed giving a modified topography, etc. The bed level is assumed not to change at the time scale of the hydrodynamics (here, 12 h 20 min). Bed-level change is computed with a morphodynamical time step (here: 100 years) using tide-averaged sediment transports. The following sections describe the components of the model and summarise test results.

2.2. Hydrodynamics

The HAMSOM model (Backhaus, 1983, 1985) solves the 3D shallow-water equations on an Arakawa-C grid (Arakawa and Lamb, 1977), with fixed levels (z-coordinates) in the vertical. Here, it is used to solve the two-dimensional (2D), depth-averaged shallow-water equations

$$\frac{\partial \zeta}{\partial t}+\frac{\partial (hu)}{\partial x}+\frac{\partial (hv)}{\partial y}=0, \tag{1}$$

$$\frac{\partial u}{\partial t}+u\frac{\partial u}{\partial x}+v\frac{\partial u}{\partial y}-fv = -g\frac{\partial \zeta}{\partial x}-\frac{C_d\sqrt{u^2+v^2}u}{h}, \tag{2}$$

$$\frac{\partial v}{\partial t}+u\frac{\partial v}{\partial x}+v\frac{\partial v}{\partial y}+fu = -g\frac{\partial \zeta}{\partial y}-\frac{C_d\sqrt{u^2+v^2}v}{h}, \tag{3}$$

where Eq. (1) is the continuity equation and Eqs. (2) and (3) are the momentum equations in the x- and y-direction, respectively. The physical effects included are conservation of mass and momentum, advection of momentum, the Coriolis force, acceleration by pressure differences and bottom shear stress. In these equations, u and v are the velocities in the x- and y-direction, t is time, f is the Coriolis parameter, g the acceleration due to gravity, C_d a drag coefficient and $h=\zeta-Z$ the water depth, with ζ the water level, and Z the bed level relative to datum (here: mean sea level).

In the first HAMSOM run the model is spun up from zero water levels and velocities. The last tidal cycle of this run is used for the first bed-level update. Subsequent runs of HAMSOM are started from the last time step of the previous model run and allowed only short spin-up to save computing time.

2.3. Sediment transport

The formulation of Bailard (1981) is used to compute bed-load transports, as described by Soulsby (1997). It follows the energetics approach of Bagnold (1963). The volumetric bed-load transport rate $\mathbf{q}$ is given by

$$\mathbf{q}=\frac{c_f\varepsilon}{g(s-1)\tan\phi_i}|\mathbf{u}_b|^2\mathbf{u}_b-\frac{c_f\varepsilon\tan\beta}{g(s-1)\tan^2\phi_i}|\mathbf{u}_b|^3\mathbf{i}. \tag{4}$$

The first term is the bed-load transport, the second term describes the effect of slopes in the bed. Bold face variables are vectors. In Eq. (4), $\mathbf{u}_b$ is the flow velocity at level a from the seabed, c_f a friction factor, $\varepsilon=0.10$ an efficiency coefficient, s the relative density of sand grains in water, ϕ_i the angle of internal friction of sediment, $0\leqslant\beta<\pi/2$ the bed slope and $\mathbf{i}$ a unity vector in the up-slope direction. The influence of grain size enters through the friction factor c_f and the efficiency coefficient ε. Here, we assume a single grain size.

The near-bottom velocity $\mathbf{u}_b$ at level a above the bed follows from assuming a logarithmic velocity profile

$$\mathbf{u}_b=\frac{\mathbf{u}_*}{\kappa}\ln\left(\frac{a}{z_0}\right), \tag{5}$$

where $\kappa=0.4$ is Von Kármán's constant, $\mathbf{u}_*$ is the friction velocity and z_0 is the roughness length. Following Soulsby (1997), the top of the bottom-boundary layer was assumed at $a=0.05$ m. The

bed-shear stress is assumed to be identical to that of the depth-averaged velocity **u**:

$$C_d|\mathbf{u}|\mathbf{u} = |\mathbf{u}_*|\mathbf{u}_* = c_f|\mathbf{u}_b|\mathbf{u}_b. \quad (6)$$

This yields for the friction factor

$$c_f = \left(\frac{\kappa}{\ln(a/z_0)}\right)^2, \quad (7)$$

and for the drag coefficient

$$C_d = \left(\frac{\kappa}{\ln(12h/30z_0)}\right)^2. \quad (8)$$

The roughness length z_0 was computed from Eq. (8), using the constant drag coefficient C_d prescribed for the hydrodynamical model. An improved value for the friction factor can be obtained if the friction law of the hydrodynamical model is improved (see also Section 1.2). The physical meaning of the present implementation is that the dimensions of small-scale bed forms (and thus the roughness length z_0) are proportional to the local water depth.

Comparison of sediment-transport formulation (4) (without the slope term) with field observations gave reasonable results for shelf-sea conditions with and without waves (Van der Molen, 2003).

2.4. Bed-level change

Changes in bed level Z are computed from conservation of sediment volume

$$\frac{\partial Z}{\partial t} = -\frac{1}{1-p}\nabla \cdot \langle \mathbf{q} \rangle. \quad (9)$$

Here, p is the porosity of the bed and $\langle \mathbf{q} \rangle$ is the tidally averaged sediment-transport vector. The bed level has negative values below mean water level.

When inserted in Eq. (9), the slope term in sediment-transport formulation (4) results mathematically in a diffusive term. This term smoothes topography as it describes down-slope sediment motion for every flow velocity, and thus has a stabilising influence on the growth of bed forms.

The continuity equation for sediment (9) is solved numerically using the method of Lax and Wendroff (1960). Details of the implementation are given in Appendix A. In case of the onset of shock waves, the solution of this method is dominated by the truncation error, and thus unreliable. To prevent shock waves, artificial stabilisation methods may be used. The method can be applied without artificial stabilisation methods when the grid size is sufficiently small (typically, about the water depth for unidirectional flow, and about ten times the water depth for tidal flow) (Appendix B). In that case the natural bed-slope terms can become larger than the truncation error of the numerical method.

2.5. Model tests

As full verification of the model results for Taylor's problem cannot be obtained, two different test cases were considered that test the main feedback mechanisms of the model: the evolution of a sinusoidal hump in stationary flow in a channel and the initial growth of alternating bars in a tidal channel.

Using the method of characteristics, De Vriend (1987) showed that the evolution of a sinusoidal hump in stationary flow can be computed analytically when slope terms in the sediment transport are neglected. In one dimension, the hump steepens while it travels in the direction of the flow. In two dimensions, the hump evolves into a three-pointed star (resembling a barchan dune), with one point oriented against the flow. The present model follows the one-dimensional (1D) solution well until the onset of a shock wave. In two dimensions, running on a grid size of about the water depth (see Appendix B), the model reproduces the three-pointed star shape, while shock-wave formation is prevented by the natural slope terms.

Using linear stability analysis, Seminara and Tubino (2001) and Schramkowski et al. (2002) demonstrated that alternating bars form in a tidal channel as a natural instability of the sediment-water system (length: 23 km, width: 500 m, M_2 current, no Coriolis effect). With the proper parameter settings, forcing and basin dimensions (Schramkowski, pers. comm.), the present model increases the amplitude of an initial alternating bar pattern. Thus, the model also shows the expected behaviour in tidal conditions.

3. Results for Taylor's problem

This section presents model results for our extension of Taylor's problem. First, an adaptation of the model for coarse grids is discussed. Next, the model geometry and the parameter settings are described. Subsequently, the morphodynamical evolution is presented for stationary sea level (Case 1), followed by results for a 10 m lower sea level (Case 2). These simulations illustrate the morphodynamic evolution of the basin and the influence of sea level. Because in reality sea level has risen during the last 18,000 years, the dynamic response to sea-level rise is investigated next (Case 3). Finally, sinusoidal sea-level variation is considered to obtain a first, crude approximation of the system's behaviour for glacial–interglacial cycles (Case 4).

3.1. Diffusion

A diffusion term was added to the sediment continuity equation to prevent the onset of shock waves, because the computational cost of a small enough grid size (Appendix B, criterion (B.4)) was prohibitive for Taylor's problem. The diffusion term can be considered to represent the combined effect of physical diffusive processes, such as slope terms on bed forms and diffusion through concentration gradients or by waves, see also Section 4.

The diffusion term was added to the right-hand side of the second step of the solution of the discretised sediment continuity Eq. (A.13):

$$-K\left(\frac{Z^k_{i+1,j}-2Z^k_{i,j}+Z^k_{i-1,j}}{\Delta x^2}+\frac{Z^k_{i,j+1}-2Z^k_{i,j}+Z^k_{i,j-1}}{\Delta y^2}\right), \tag{10}$$

where K is a constant diffusion coefficient and indices i,j,k denote grid positions in the x- and y-direction and the time level, respectively.

The magnitude of the diffusion is known by specifying the diffusion coefficient K, and its role in the model solution is analysed below. Such insight is important for (near) morphodynamical equilibrium, where diffusion inevitably plays a role.

3.2. Geometry and parameter settings

The model geometry is shown in Fig. 2A. The geometry consists of a shallow basin in the south and a deep basin in the north. Only the northern boundary is open. The shallow basin has the average depth of the Southern Bight of the North Sea (25 m) and the northern basin that of the North Sea (75 m). The transition between the basins is sinusoidal. The width of both basins approximates the width of the Southern Bight (165 km). The length of each basin is half the M_2 wavelength, as determined by the depth (i.e., 340 and 600 km, respectively). Thus, each basin

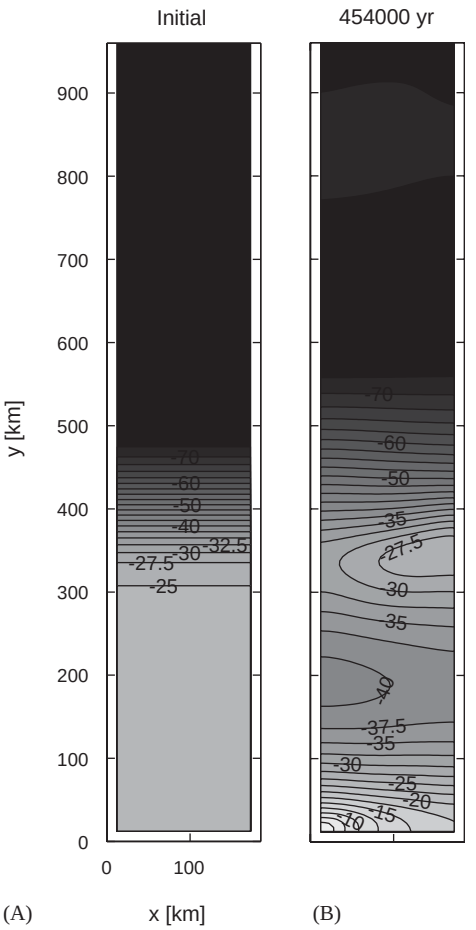

Fig. 2. Bathymetry of Taylor's problem, Case 1. (A) initial bathymetry; (B) bathymetry after 454,000 years. Contour interval 2.5 m.

accommodates an amphidromic system. The grid distance is 5 km and the basin is located at 52° N (i.e., $f = 1.15 \times 10^{-4}/s^{-1}$). The southern basin is the area of interest, while the northern basin buffers deviations between boundary conditions and internal hydrodynamics. The initial bathymetries of both basins are flat bottoms in all simulations. A sensitivity study with various initial bottom topographies invariably showed evolution towards the same situation. The basin geometry preserves the main physics of the tidal system of the southern North Sea. The model cannot resolve local morphology such as tidal sandbanks.

The northern boundary was forced with M_2 tidal water levels with a 12 h period. The boundary condition was the superposition of an incoming and an outgoing Kelvin wave. The Kelvin waves had an amplitude ratio of 0.2, as expected for Taylor's problem with friction (Zheng et al., 1991). The water levels along the boundary were in phase, corresponding to a position between two amphidromic points (Taylor, 1920). The amplitude of the incoming Kelvin wave (1.9 m) was chosen to yield realistic flow velocities in the southern basin. A radiative boundary condition was selected to limit reflection back into the basin (see Backhaus, 1983, 1985 for details). The same open-boundary conditions were prescribed for all the simulations, and independent of time. This assumption is rather crude because the tidal wavelength depends on the depth. Also, changes in the seabed topography will alter the reflection of the tide in the south. The radiative boundary condition cannot fully compensate for misfits between the open-boundary condition and the internal hydrodynamics of the model. Thus, some tidal energy will reflect back into the basin and affect the morphodynamical evolution. Only the speed of the morphodynamical evolution is affected, because the reflected tide alters only the amplitudes of water levels and currents.

The hydrodynamical model had a time step of 300 s and a time and space invariant drag coefficient $C_d = 2.5 \times 10^{-3}$. The central advection scheme of HAMSOM was selected. The initial spin-up period was 14.5 days, subsequent runs had a warm restart with 2.5 days spin-up to adjust to the new bed levels. The subsequent (last) 12 h of each run were used to compute new bed levels. Hydrodynamics were stored every 600 s.

The morphodynamical model had a time step of 100 years. The diffusion coefficient was $K = 3.25 \times 10^{-4}\,m^2/s$. This value was selected using sensitivity runs to be just large enough to prevent the onset of shock waves in the solution for the seabed. The bed-slope term was excluded, because only small bed slopes could develop given the large grid size. The sediment-transport formulation uses the same roughness coefficient as the hydrodynamical model. The relative density of sediment in water was $s = 2.65$, representative of quartz sand. The internal friction coefficient was $\tan \phi_i = 0.63$.

All simulations were continued as long as possible with the aim of getting as near to an equilibrium state as possible, if it exists. The runs were stopped when grid cells emerged above local low-water level. Longer simulations might be possible if the model would allow for flooding and drying. For the hydrodynamical model, an elegant solution is available (Stelling and Duinmeijer, 2003) that might work well for morphodynamical computations. It may be more difficult to improve the morphodynamical routine because of the relationship between grid size and water depth (Appendix B).

3.3. Case 1: present sea level

3.3.1. Bed-level evolution

The bathymetry after 454,000 years of morphodynamical evolution is shown in Fig. 2B. Longer simulation was impossible because the seabed emerged in the southwest corner.

Overall, the depth of the southern basin has increased. The eroded material has been deposited mostly on the slope to the northern basin. The slope has accreted towards the north and has become less steep. In addition to the general deepening, sediment has been deposited near the southern model boundary, in particular on the western side. The central southern basin has deepened to about 40 m, slightly more in the west than in the east. To the north, a shallow area has developed, with emphasis on the eastern side (about 27 m). Model results without the Coriolis

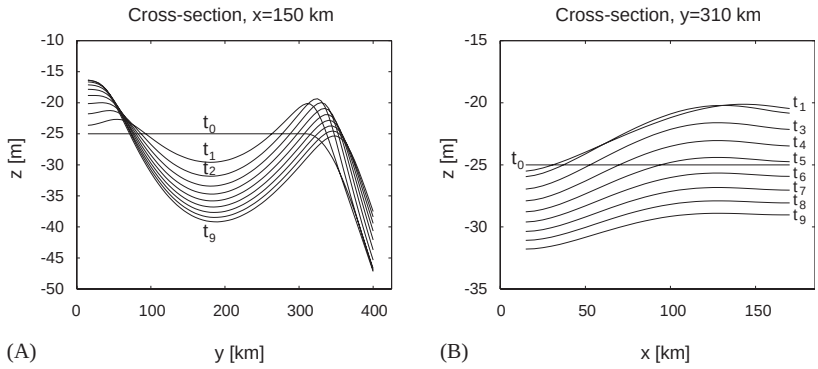

Fig. 3. Cross-sections Case 1. (A) At $x = 150$ km in y-direction. (B) At $y = 310$ km in x-direction. Profiles every 50,000 years.

force showed no east–west bottom structure, identifying the amphidromic system as its cause.

Profiles taken every 50,000 years at two cross-sections illustrate the temporal evolution (Fig. 3). The north–south cross-section (Fig. 3A) shows that the rate of evolution decreases fairly rapidly in time, with the main bathymetrical features developing within the first 100,000 years. The shallow area in the north ($y \approx 320$ km) first builds up, and then moves northward down the slope. Near the southern boundary ($y \approx 20$ km), the accretion gradually slows down until it nearly stops. The cross-section in the x-direction (Fig. 3B) shows the initial accretion of the northern shoal (50,000 years). Subsequently, the bed levels decrease as the shoal moves away to the north.

The emerging grid cells indicate that the model problem has the potential to develop intertidal areas and shores by itself. This result corresponds with real-world situations, and is worth further investigation with a model that is capable of flooding and drying, specifically to establish the fate of such coastal areas as the evolution of the basin continues.

Below, the hydrodynamics and sediment-transport patterns are analysed for the initial and final situation to obtain a physical understanding of the bottom evolution.

3.3.2. *Analysis initial state*

Sediment is transported by asymmetry of the tidal currents, residual currents, and diffusion. These processes are fully accounted for by internal generation (asymmetry and residuals) or prescription (diffusion) in the model. To analyse the main contributions of these processes, the hydrodynamics generated by the model at various stages of the morphodynamical evolution were post-processed. This was carried out by harmonic analysis of stored time series of water levels and currents, and by recalculating the main components of sediment transport and bed-level change.

A decomposition of the hydrodynamics for the initial bathymetry is given in Fig. 4. The co-tidal chart of the M_2 water levels (Fig. 4A) shows an amphidromic system in each of the basins. The amphidromic points are displaced to the east by frictional dissipation and energy transfer to overtides in accordance with earlier results (Rienecker and Teubner, 1980; Zheng et al., 1991). Thus, water-level amplitudes are larger in the west than in the east.

As the M_2 tide moves through the basin, energy is transferred by non-linear processes to higher harmonics (overtides) (see, e.g., Parker, 1991), causing tidal asymmetry. The most important overtide is M_4, with twice the frequency of M_2. The co-tidal chart of the M_4 water levels (Fig. 4B) shows four amphidromic systems as expected. M_4 increases in amplitude as it is generated along the path of M_2 through the basin. Hence, the amphidromic points of M_4 are located more to the west in the north than in the south.

Co-tidal charts of the currents of M_2 and M_4 are given in Fig. 4C and D. Asymmetry of the tide caused by M_2 and M_4 provides an important

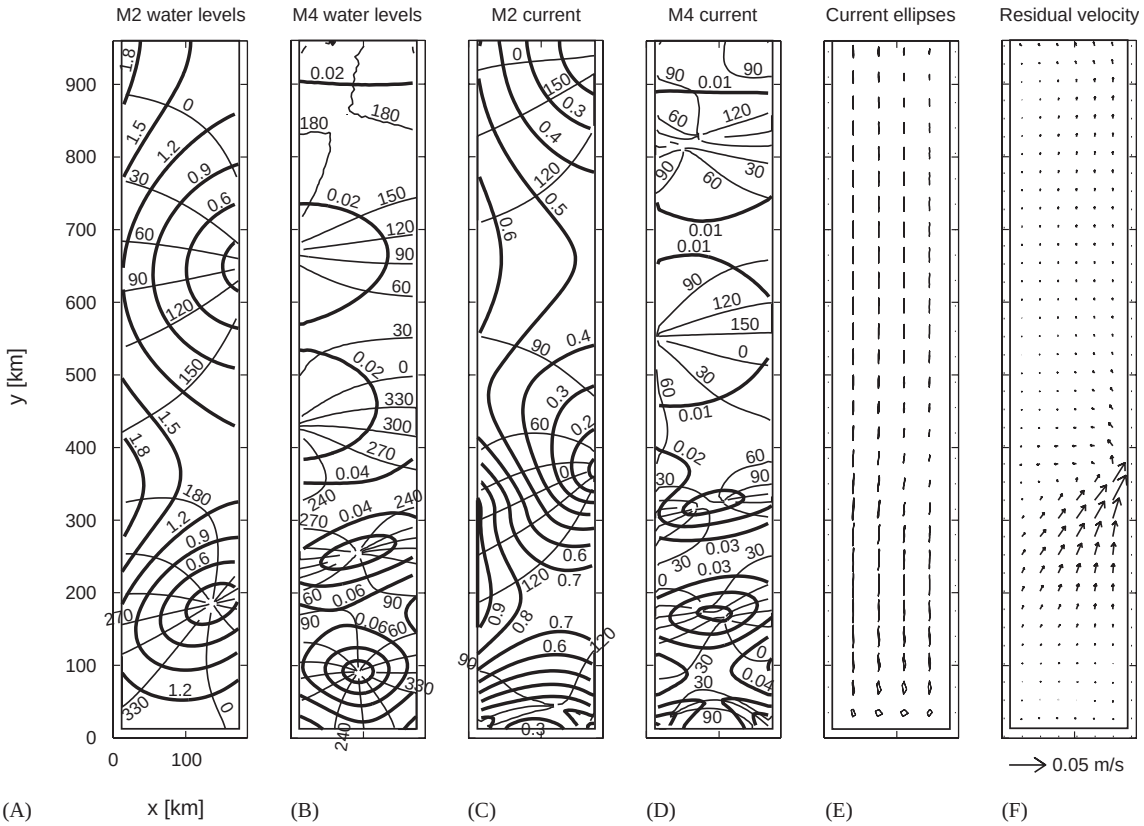

Fig. 4. Hydrodynamics for Case 1, initial bathymetry. (A) Co-tidal chart, M_2 water levels; (B) co-tidal chart, M_4; (C) co-tidal chart, M_2 currents; (D) co-tidal chart, M_4 currents; (E) tidal current ellipses; and (F) residual velocity.

contribution to the tide-averaged sediment transport (e.g., Van de Kreeke and Robaczewska, 1993). The currents show the same characteristics as the water levels. The main difference is that the amphidromic points are grouped in pairs between the water-level amphidromic points, in accordance with theory (Xia et al., 1995). Thus, the central pair of M_4 current amphidromic points nearly coincides with the M_2 water-level amphidromic point. The largest tidal current asymmetry is expected between the (pairs of) M_4 current amphidromic points where the M_4 currents are large. The phase differences between M_2 and M_4 also play a role, however, as will be discussed further on.

The current ellipses (Fig. 4E) are oriented along the axis of the basin, except near the southern boundary where the ellipticity is large. These results correspond with the frictionless results of Taylor (1920), but not with those with friction by Zheng et al. (1991). They report a clockwise rotation of the current ellipses in the area near the southern boundary. This difference was not further investigated because the ellipses in the present model correspond well with more realistic model results (e.g., Pingree and Griffiths, 1979; Davies and Kwong, 2000). Sediment is expected to be transported mainly with the currents along the north–south direction.

Residual currents induced by the tide also cause net sediment transport. Such currents are caused by differences in mean sea level (geostrophic balance), mass transport by the Kelvin wave (Stokes drift), and topographic gradients (rectification). The model generates residual currents of a few cm/s to the north in the northern half of the

southern basin (Fig. 4F). The magnitudes increase to the north and east. The currents have a considerable eastward component. The residual current pattern resembles results by Pingree et al. (1984). Their 1D model showed seaward residual currents seaward of the M_2 tidal node and negligible currents landward of the node. The currents are generated mainly by continuity (Stokes drift). Here, the pattern is modified by tidal amplitude differences and earth rotation.

The initial tide-averaged volumetric sediment transport per unit width is decomposed in Fig. 5. The bed-load transport is oriented mainly along the basin axis (Fig. 5A). A bed-load parting zone occupies the centre of the southern basin, which is eroded. The transport magnitudes decrease further to the north and south of the parting, resulting in deposition. The largest accretion occurs in the southwest and northeast. Sediment is also transported down the slope to the northern basin, resulting in the export of the sediment.

Decomposition into residual current and tidal asymmetry components (Fig. 5B) was carried

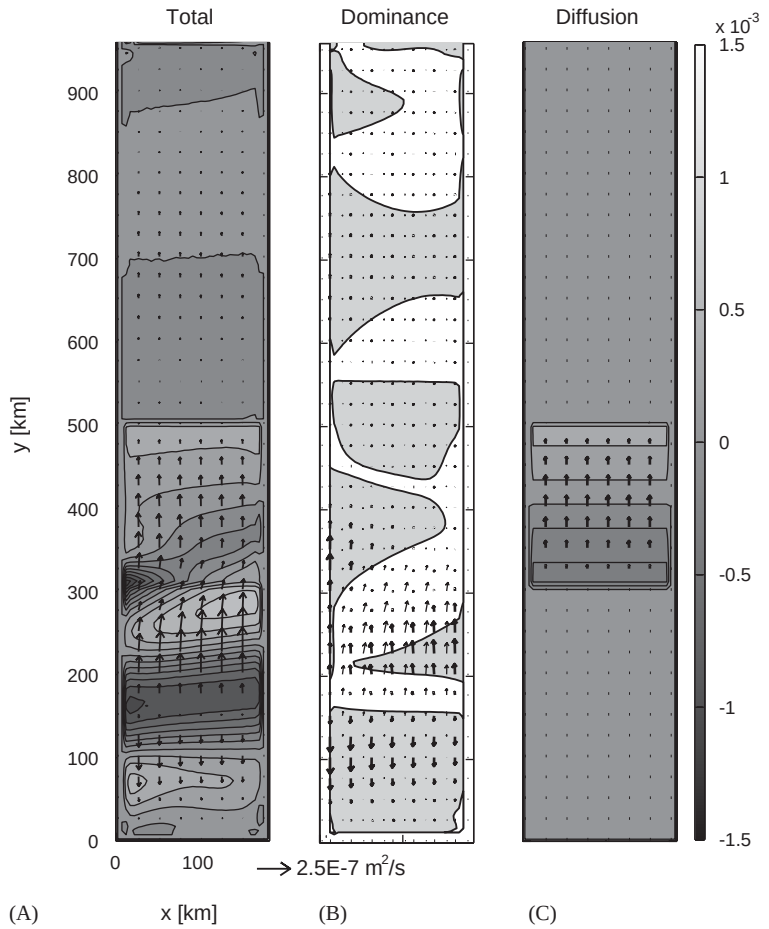

Fig. 5. Sediment transport, Case 1, initial bathymetry. (A) Bed-load transport (arrows) (m^2/s) and rate of bed-level change (gray tones) (mm/year). (B) Contribution to bed-load transport by tidal asymmetry (thick arrows) and residual current (thin arrows), and areas where transport by tidal asymmetry is larger (gray) or where transport by the residual current is larger (white). Arrows are plotted at alternating locations for the sake of legibility. (C) Contribution to the total transport by the diffussion, symbols as for (A).

out using

$$\langle q_x \rangle = \frac{c_f \varepsilon}{g(s-1)\tan\phi_i}[u_0^3 + u_0 v_0^2 + \frac{3}{2}u_0 u_2^2 + \frac{1}{2}u_0 v_2^2 + v_0 v_2 u_2 \cos(\beta_x - \beta_y) + \frac{3}{2}u_0 u_4^2 + \frac{1}{2}u_0 v_4^2 + v_0 v_4 u_4 \cos(\gamma_x - \gamma_y) + \frac{3}{4}u_2^2 u_4 \cos(2\beta_x - \gamma_x) + \frac{1}{2}v_2 u_2 v_4 \cos(\beta_x + \beta_y - \gamma_y) + \frac{1}{4}v_2^2 u_4 \cos(2\beta_y - \gamma_x)], \quad (11)$$

with an equivalent expression for the y-direction (Van der Molen and De Swart, 2001). All velocities are at $a = 0.05$ m above the bed as before (subscripts b have been dropped for brevity) and were obtained by harmonic analysis. Subscripts 0, 2 and 4 denote the residual current, the M_2 tide, and the M_4 tide, respectively. The phase angles β and γ are of the M_2 and M_4 components, respectively. The first eight terms are the transport involving the residual current, the last three terms that by the tidal asymmetry.

The bed-load parting (Fig. 5B) is caused by tidal asymmetry, while the northward transport is enhanced by the residual current. The divergence by tidal asymmetry is caused by the amphidromy of the M_2 and M_4 currents (Fig. 4C and D). In the bed-load parting zone the phase of the M_2 currents is nearly constant, while that of the M_4 currents takes all possible values. This causes ebb dominance in the northwest and southeast, and flood dominance in the northeast and southwest (ninth term in Eq. (11)). The phase of the M_4 current is nearly constant between the (pairs of) M_4 amphidromic points. There the magnitude of M_4 determines the magnitude of the transports. The pattern of transport by tidal asymmetry compares well with the phase relationship between M_2 and M_4 currents of Pingree et al. (1984). Their analytical expressions and 1D shelf model showed flood dominance between the M_2 elevation node and the reflective coastal boundary, and ebb dominance seaward of the node. This result corresponds to the western side of the basin, but also to the eastern side of the basin when accounting for the propagation direction of M_2. The same general asymmetry structure linking M_2 and M_4 amphidromy to a bed-load parting is also present in the English Channel and the Irish Sea (Pingree and Griffiths, 1979). Comparison of computed M_2 co-tidal charts (Lee and Jung, 1999) with computed sediment-transport rates (Zhu and Chang, 2000) for the Yellow Sea does not show the same pattern, because tidal currents are too weak to move much sediment in the region where well-developed amphidromic systems are present.

The magnitude of the flux involving the residual current does not vary much across the basin, in contrast to the residual current itself. The cause is the opposite trend of the magnitude of the M_2 current (third and fourth terms in Eq. (11)). As expected, the transport contribution involving the residual current is slightly eastward. The contribution by tidal asymmetry is the largest in the south, while the residual current contributes most in the northwest and also at the bed-load parting (gray tones).

The transport by diffusion (Fig. 5C) was computed directly from the gradients in the bed topography. This contribution is initially zero where the bottom is flat. On the slope to the northern basin it is dominant. Thus, the diffusion contributes to the export of sediment. It also causes the reduction in the slope gradient.

3.3.3. *Analysis final state and comparison with initial state*

After 454,000 years, the amphidromic system of the M_2 water levels has shifted to the north (Fig. 6A). The shift is caused by the increase in depth, which causes a larger tidal wavelength. The wavelength in shallow water is $\lambda = T\sqrt{gh}$ (e.g., Gill, 1982), with T the wave period. A change in water depth from $h_1 = 25$ m to $h_2 = 30$ m shifts the amphidromic point northward by $\Delta\lambda/4 = \frac{1}{4}T(\sqrt{gh_2} - \sqrt{gh_1}) \approx 17$ km, in good agreement with the model results. Likewise, the northern amphidromic system of M_4 is shifted to the north (Fig. 6B). It is also shifted to the deeper west, where less M_4 is generated. The southern M_4 amphidromic system is shifted to the west, because

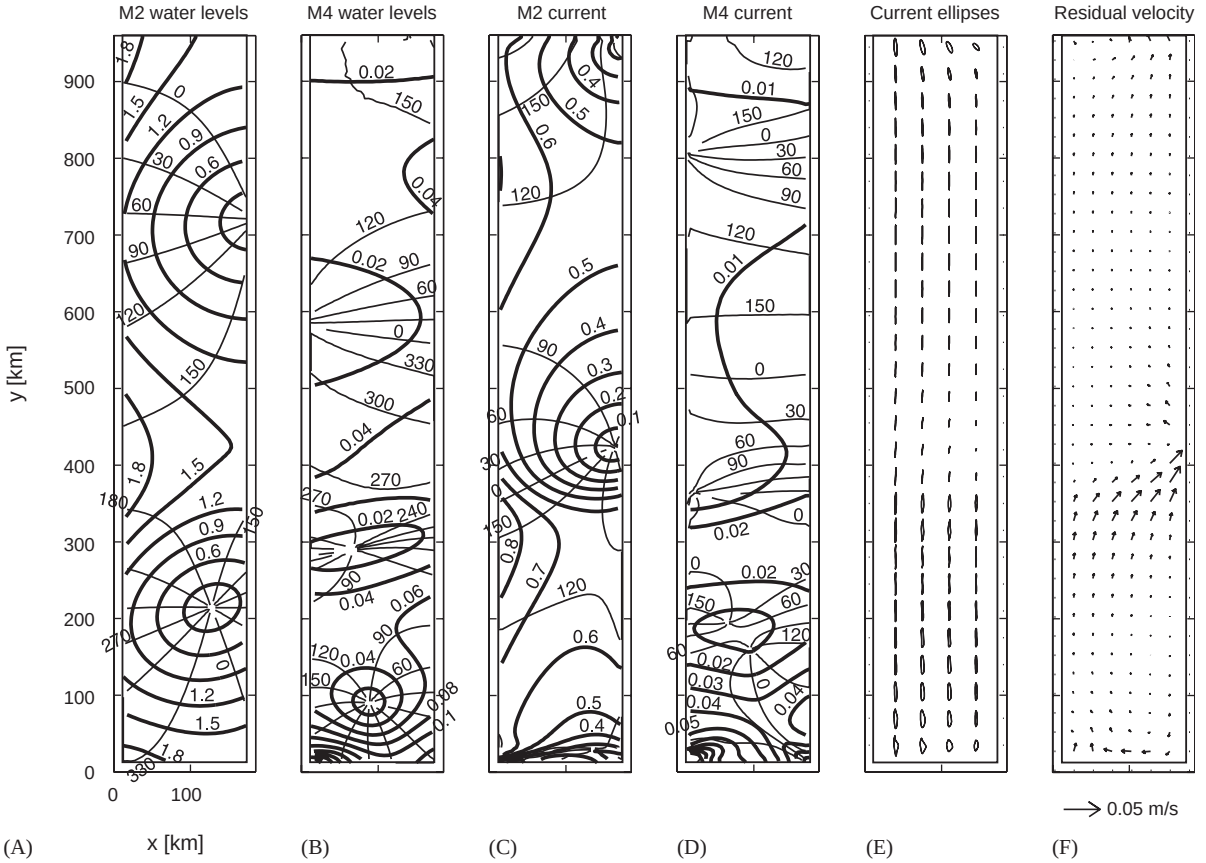

Fig. 6. As for Fig. 4, at $T = 454,000$ years.

the reflected M_4 Kelvin wave is enhanced by generation along the shallow southern boundary.

The changes in the current amphidromic systems of M_2 and M_4 are similar to those of the water levels (Fig. 6C and D). In addition, the M_2 currents are smaller because of the increased depth. The M_4 currents have decreased similarly. Also, their generation is reduced. The amphidromic pair in the central southern basin has separated along a northwest to southeast axis. This separation is most likely caused by generation of M_4 on the shoals in the southwest and northeast. The current ellipticity is increased, in particular in the south (Fig. 6E). This increase is possibly caused by partial reflection of the tide on the bathymetry, which excites Poincaré waves. Additional residual currents are generated at the slope in the south (Fig. 6F). The field of residual currents in the north has followed the northward shift of the slope to the northern basin. Their amplitudes have decreased.

After 454,000 years, the net bed-load transport (Fig. 7A) has decreased. Sediment transports in the south have nearly vanished. In the north, sediment is still exported. The decomposition (Fig. 7B) shows particularly smaller transport by tidal asymmetry. The bed-load parting now has a more northwest–southeast orientation. The smaller transport by tidal asymmetry is caused by smaller current amplitudes of both M_2 and M_4. The rotation is caused by the separation of the pair of M_4 current amphidromic points (Fig. 6D). The transport involving the residual current is also smaller, except in the northwest, because there the residual current has increased and the M_2 current has reduced only slightly.

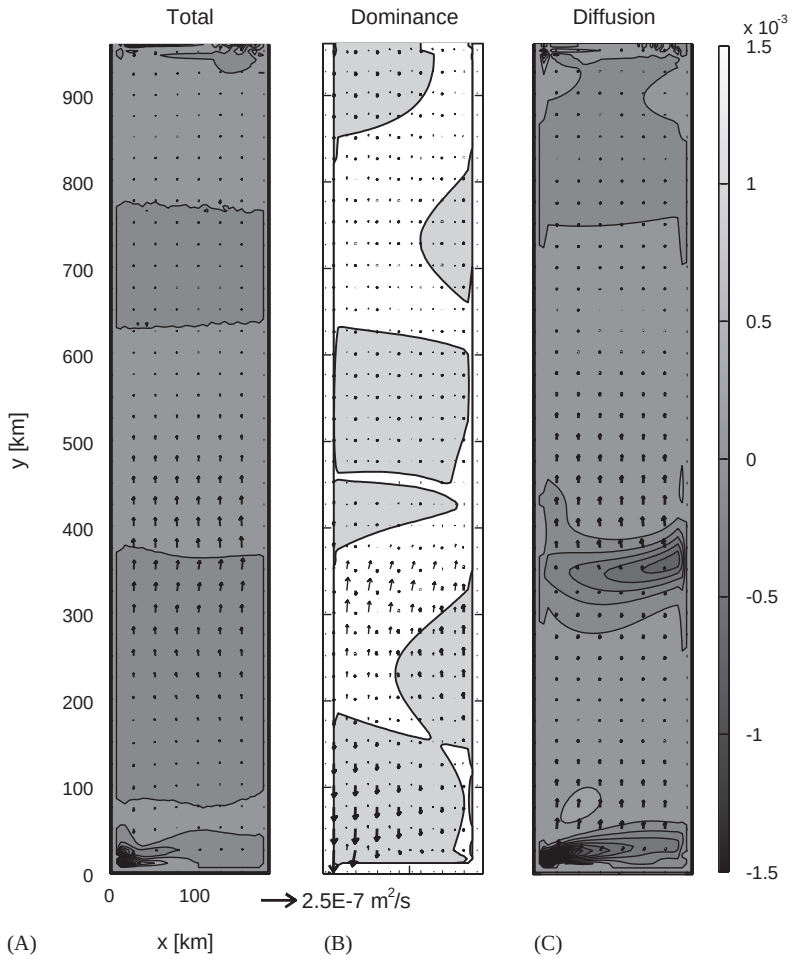

Fig. 7. As for Fig. 5, at $T = 454,000$ years.

The transport by diffusion (Fig. 7C) still dominates on the slope to the northern basin. In addition, it now counteracts the northward transport in the north, and it nearly cancels the southward transport in the south. The latter results in conditions near equilibrium (see also Fig. 3A). Thus, the diffusion retards the development, and limits bed-level gradients. Overall, however, the diffusion term is too small to alter the qualitative behaviour of the model.

3.4. Case 2: 10 m lower sea level

Results of 42,000 years of evolution for a 10 m lower sea level are shown in Fig. 8. Only relevant elements of the initial situation are analysed, as trends during the simulation were similar to Case 1.

The final bathymetry (Fig. 8A) shows the same pattern as in Case 1 (Fig. 2B). The main difference is that the bed-level pattern has a smaller wavelength. This reduction is caused, as before, by a smaller tidal wavelength, associated with the smaller depth. The smaller wavelength causes a southward shift of the amphidromic system (Fig. 8B). This shift results in smaller M_2 tidal currents in the east than in the west. As a result, M_4 currents (Fig. 8C) are now generated mostly in the west. The M_4 tide is dissipated considerably before it reaches the eastern side of the basin.

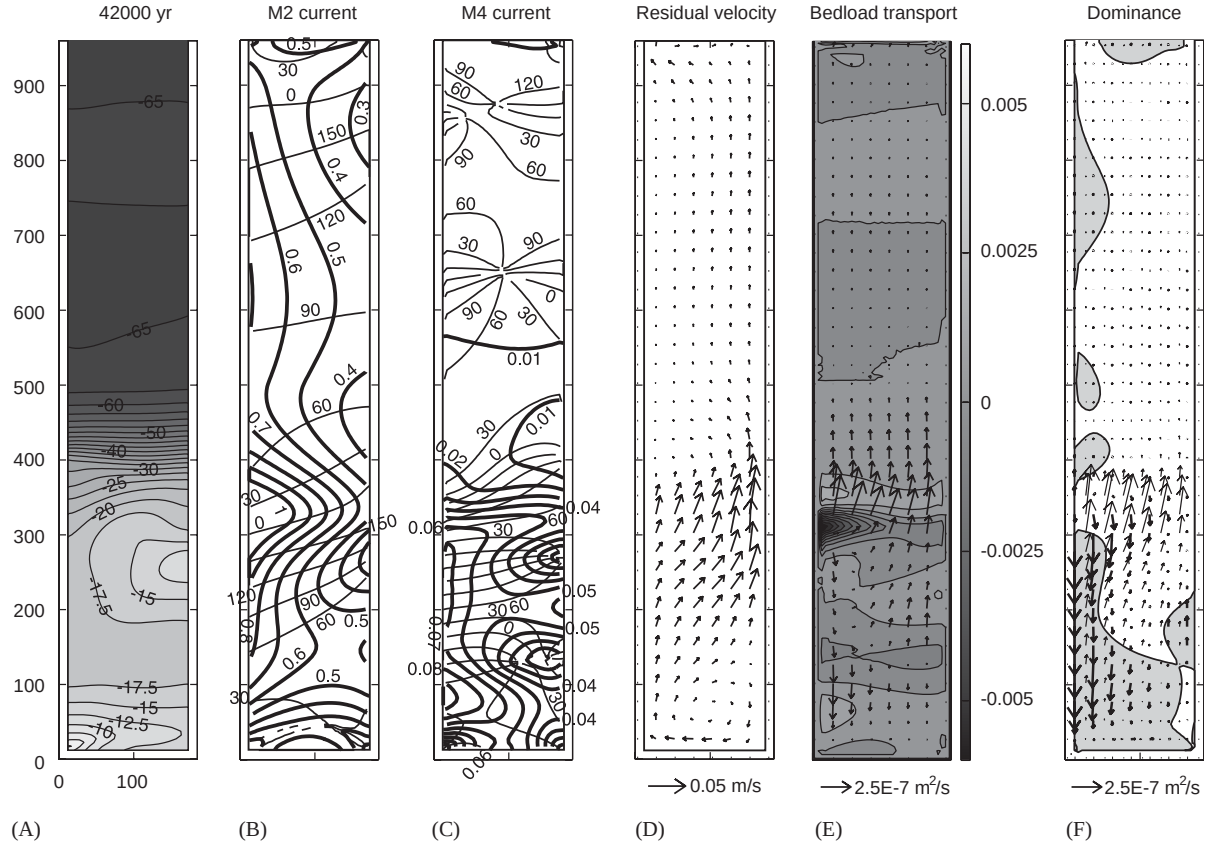

Fig. 8. Final bathymetry and initial hydrodynamics and sediment transport for Case 2. (A) Bathymetry at $T = 42,000$ years, contour interval 2.5 m. (B) Co-tidal chart, M_2 currents, $T = 0$. (C) Co-tidal chart, M_4 currents, $T = 0$. (D) Residual currents, $T = 0$. (E) Bed-load transport (m^2/s) and rate of bed-level change (mm/year), $T = 0$. (F) Transport decomposition, symbols as in Fig. 5.

The residual currents (Fig. 8D) are stronger than in Case 1 (Fig. 4F), and now occupy the entire southern basin. A residual circulation cell is present in the south-eastern corner. The rest of the pattern is similar to Case 1, with current directions to the northeast and larger amplitudes in the east than in the west.

The bed-load transport (Fig. 8E) shows large export of sediment on the slope to the northern basin. Sediment is also transported northward in the northeast, whereas transports are to the south in the west and south. The resulting bed-level change has the familiar pattern with a smaller wavelength. The top of the slope to the northern basin is eroded heavily, especially in the northwest where the transport direction diverges. Decomposition of the transport field (Fig. 8F) shows southward transport by tidal asymmetry in the west (flood dominant) and very small transports in the east. Along the eastern boundary, the small patch of northward transport by the tidal asymmetry contributes to the formation of the shallow area in the northeast. The transports involving the residual current are to the north, with largest values in the west, and magnitudes increasing to the north. The eastward component is more pronounced than in Case 1 and contributes to the formation of the shoal in the northeast. Overall, the residual current exports sediment from the southern basin, while the tidal asymmetry imports sediment.

Simulations were carried out also for sea levels of $+5$, -5, and -15 m. The trends were similar to those described above. For the -15 m situation,

dissipation of the tide in the southern basin was so strong that sediment transports were significantly reduced in the south.

3.5. Case 3: linear sea-level rise

Two simulations were carried out with constant rates of sea-level rise to assess the dynamic response of the system. The simulations started at a sea level of −15 m and finished at +5 m, with rates of 0.25 and 1.0 mm/year (simulation periods 80,000 and 20,000 years). Because the model contains bed-load transport only, and neglects the effects of waves and wind-driven currents, the model response represents a realistic response to 2–4 times larger rates of sea-level rise. During the Holocene, rates of sea-level rise along the eastern shores of the Southern Bight have decreased from about 10 to 1 mm/year (see, for an overview, Kiden et al., 2002). The results of the model runs are compared with a simulation at a stationary sea level of +5 m with a simulation period of 80,000 years.

The bed-level pattern of the 0.25 mm/year case (Fig. 9B) is located slightly more to the south than for the stationary sea level (Fig. 9A). Also, the top of the northern shoal is shifted to the east. This difference is expected, because the dynamic result was generated partly at lower sea levels. The 1.0 mm/year case (Fig. 9C) has smaller bed-level amplitudes, mainly because it contains less time. The wavelength is shorter than for 0.25 mm/year, indicating that non-linear processes are important and that the model response is slow.

In conclusion, sea-level rise is important for the bed-level evolution in the model. For time-varying rates of sea-level rise, the shape of the curve may also be important. For decreasing relative sea-level rise as during the Holocene, the bed-level change for higher sea levels will be more important than in the cases considered here.

3.6. Case 4: sinusoidal sea-level variation

In this last case, the response of the basin to sinusoidal sea-level forcing is investigated. The period was 30,000 years, and the range from −5 to +10 m. The simulation started in low stand. In addition, a triangle with sides of 50 km was cut off the southwest corner of the basin to postpone emergence. These settings allowed for nearly six full sea-level cycles before local emergence of the bed stopped the computation. Realistic glacial/interglacial cycles have a period of about 100,000 years, sea-level changes of about 100 m (implying dry conditions in the North Sea most of the time), rates of sea-level rise larger than those of sea-level fall, and high stands are lower. Thus, the model captures only the principle behaviour for rising and falling sea level.

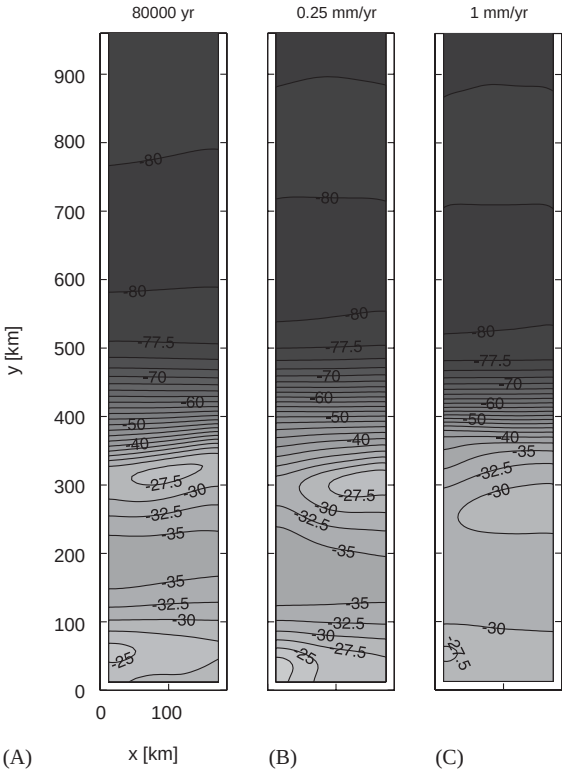

Fig. 9. Final bathymetries, Case 3. (A) For stationary sea level at +5 m, $T = 80,000$ years. (B) For sea-level rise 0.25 mm/year, from −10 to +5 m, $T = 80,000$ years. (C) For sea-level rise 1 mm/year, from −10 to +5 m, $T = 20,000$ years. Contour interval 2.5 m.

The general trend in bed-level evolution resembles that of the previous cases. The temporal evolution, however, is different. Cross-sections of the bed level taken every 3000 years (Fig. 10A) show clustering typical for sedimentary systems

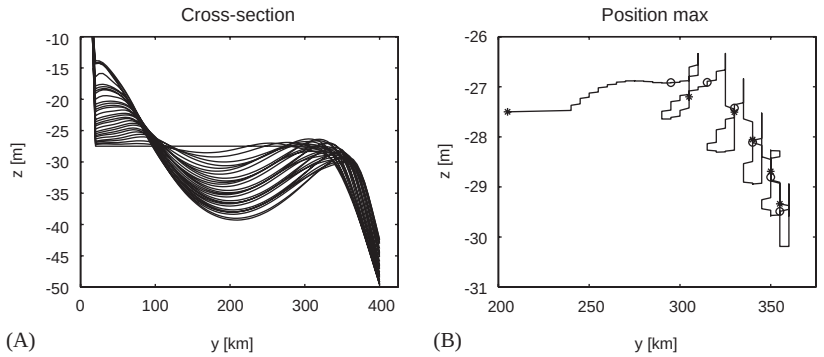

Fig. 10. Results for sinusoidal sea-level change, period 30,000 years. (A) Cross-sections of bed level at $x = 55$ km, plotted every 3000 years. (B) Position of the top of the shallow area between the two basins through time. Asterisks: sea-level low stands; circles: sea-level high stands.

subject to periodical forcing. This behaviour is caused by both sea-level-dependent rates of development, and spatial oscillations in the pattern of bed-level change caused by tidal wavelength variation. These effects are illustrated by the position of the maximum of the northern shoal (Fig. 10B). The initial position is at the left-most asterisk, and subsequent positions in time follow the line. Asterisks indicate the moments of low stand and circles indicate high stands. On average, the shoal accretes first, and then moves down the slope to the northern basin. Superimposed on this trend, the shoal accretes and advances around high stands, and erodes and retreats around low stands. Clearly, the advance and retreat follow the motion of the deposition zone across the top of the shoal as sea level oscillates, and with a substantial phase lag (nearly 90°). Throughout the process, sediment is exported to the north across the shoal (see Figs. 5A and 8E). The phase lag indicates that the system is quite inert. The erosion is caused partially by diffusion. For lower sea levels, and for oscillations with a longer period, the system response will be faster, and the top of the shoal will follow the forcing more closely.

4. Discussion and conclusions

4.1. Summary of results

In all the simulations, the southern basin became deeper, because residual currents and tidal asymmetry export sediment (aided by the diffusion). Also, the seabed developed a shallow area in the north, a deep area in the centre, and a shallow area against the southern boundary. This pattern is caused by the typical structure of the amphidromic system of the tidal currents. The deepening causes an increase of the tidal wavelength. As a result, the shallow area in the north is pushed down the slope into the northern basin. For oscillating sea level the northward motion is less, because the largest changes appear around low stands. Then, the northern area of deposition is located to the south of the slope to the northern basin, and export of sediment is reduced. The feedback of the developing bed levels to the water motion seems to be dominated by the mean depth increase, and much less by the superimposed and developing seabed topography.

4.2. Comparison with the realistic situation

Compared to the Southern Bight of the North Sea, the model results for Case 1 show differences caused by the Strait of Dover, the coastline geometry, and the seabed topography. Such differences may be expected, as the model contains major simplifications with regard to geometry (semi-enclosed basin), hydrodynamics (only tides), and sediment transport (bed-load, uniform grain size, no critical velocity of erosion). The advantage of this 'bottom–up approach' is that it allows investigation of the basic physical processes involved in shaping shelf-sea basins. Other important

processes (e.g., waves, sediment grading and suspension, Strait of Dover, etc.) can be added at a later stage. The differences and possible implications for the basin evolution are discussed below.

In reality, the M_2 amphidromic system of water levels is located more to the west (Prandle, 1980) than in the model, because of the Kelvin wave entering through the Strait of Dover (Prandle et al., 1993). As a result, the tidal range in the west is larger in the model than in reality (up to 1.2 m, compared to 0.9 m), smaller in the east (0.3 and 0.6 m, respectively), and smaller in the south (1.2 and 1.8 m, respectively). The phases compare well (within 30°). The amphidromic systems of M_4 are also located more to the west in reality. The southernmost amphidromic point is degenerate and located to the west of Dover. These more westerly locations are most likely caused by M_4 tidal energy entering through the Strait of Dover, and by stronger generation of M_4 in the east than in the west. Overall, the amplitudes of M_4 are smaller than in reality: up to 0.1 m in the east compared to over 0.15 m, and about 0.4 m in the west compared to 0.5 m. The phases are about 30° earlier than in reality. In the model, the southernmost amphidromic system is more prominent than in reality. The stronger generation of M_4 in reality is caused by the realistic bathymetry, which is shallow in the east. Simulations in a realistic model geometry by Xia et al. (1995) showed an M_2 current amphidromic point northeast of the Southern Bight, and another near the Thames estuary. The northern point is located slightly more to the west than in our model. The southern one is located much more to the west, presumably because of the Strait of Dover. The magnitudes of the M_2 tidal currents are approximately 0.1 m/s less than in their model, and are substantially less towards the southern model boundary. The phase of the currents in our model is about 30° later. The influence of the Strait of Dover on the morphodynamical evolution of the Southern Bight of the North Sea is an interesting topic for further research.

In reality as well as in the model, the current ellipses are aligned with the central basin axis (e.g., Davies and Kwong, 2000). This axis curves to the southwest, parallel to the coasts of the Southern Bight. The ellipticity is greater than in the model. The velocities do not vanish in the south because of the Strait of Dover. The realistic tidal residual velocities are to the north and northeast as in the model, and are largest in the northern part of the Southern Bight (Prandle, 1978). In contrast to the model, their amplitude is largest near the central basin axis. The overall amplitudes in the present model are approximately 0.01 m/s less. In Prandle's (1978) model, the residual currents do not vanish in the south because of the Strait of Dover, but they do decrease in magnitude.

In summary, the model represents the tides quite well. The tidal system is shifted to the east, mainly because of the closed southern boundary.

Comparing the sediment transport and bed-level change (Case 1) to observations (Johnson et al., 1982) and previous realistic model results (Pingree and Griffiths, 1979; Gerritsen and Berentsen, 1998; Van der Molen and De Swart, 2001), the bed-load parting and the erosion in the centre and deposition in the north are clearly reproduced. The deposition in the south is less clear in the realistic models, probably because of the Strait of Dover. The time scale of the model seems substantially longer than in reality: in about 50,000 years, the northern shoal has accreted by about 5 m, whereas in reality, 5–20 m of sediment has been deposited during the Holocene (10,000 years) (Harrison et al., 1987). The decomposition of the sediment transport into components caused by tidal asymmetry and residual current at 454,000 years matches better with the realistic situation than the initial situation. In particular, the northwest to southeast orientation of the bed-load parting is better reproduced, as well as the larger zone of northward transport by the tidal asymmetry in the northeast. The same holds for the increase of transport by the residual current from east to west in the north. This better match may result from the more westward location of the amphidromic systems at 454,000 years or from the bed topography. A model experiment with a flat bottom and less friction showed a more westward location of the amphidromic point, but not the rotation of the bed-load parting. Thus the rotation is caused by the seabed topography. The comparison also suggests that the eastern boundary of

the present model should be projected along the eastern shore of the Southern Bight up to the Strait of Dover (the Dutch island of Texel being located at about $y = 300$ km). The southern boundary represents the section from Calais to the mouth of the river Thames.

The seabed topography generated by the model does not match the real bathymetry, despite the agreement with observations and realistic model results. The actual bathymetry (e.g., Caston, 1979) is shallow in the Thames Estuary (depths less than 20 m), and in the east (depths less than 30 m). In the west, depths are about 40 m. At the transition to the deeper North Sea to the north (depths >40 m), water depths are relatively small (~ 30 m) across the entire width of Southern Bight. Qualitatively, a shallow area at the transition to the northern basin evolves in the model. Also, the model generates a shallow area where the Thames Estuary might be projected. In reality, the latter is at least partly the result of fluvial processes. Also, the deepest areas in the model are in the west, in correspondence with reality. The model does not generate, however, a shallow area in the east along the entire length of the basin.

The present bathymetry of the Southern Bight of the North Sea was formed mainly by marine and glacial processes (Banner, 1979). During the Saalien ice age (the second last) the British and Fennoscandian ice sheets reached the north of the Southern Bight, forming ice-pushed ridges and glacial drainage valleys (Oele and Schüttenhelm, 1979). In the Eemian (the subsequent interglacial), marine processes redistributed sediment, resulting in deposits with a similar spatial distribution as those of the Holocene (Cameron et al., 1984b; Cameron et al; 1986). The ice sheets of the Weichselian ice age (the last one) did not reach the region, and limited bathymetric changes were caused by aeolean and fluvial processes (Jelgersma et al., 1979). Large amounts of sediment were displaced during the Holocene, resulting in 5–20 m thick deposits in the east and north, probably originating from the west where Holocene sediments are nearly absent (combined maps of Cameron et al., 1984a; Harrison et al., 1987; Balson, 1988; Balson and D'Olier, 1990; Balson et al., 1991). The eastern coast-line has made a large shift during the Holocene sea-level rise, and coastal processes (wave action) have played an important role in the formation of the eastern deposits. The early Holocene sediment consist of peat and clay, however (Jelgersma et al., 1979). Sediment supply by the river Rhine (the largest river in the area) was limited during the Holocene (Beets and Van der Spek, 2000). Erosion resistive material (gravel) in the west and near the Strait of Dover (Balson, 1988; Balson and D'Olier, 1990) will have influenced the evolution by limiting erosion locally, and, by resulting reduced sediment supply, limiting deposition elsewhere. In addition, it may have sped up the migration of large-scale bed features that would otherwise have accumulated further, and hence would have been more inert. Comparison of the morphodynamical evolution in the model with the distribution of Holocene sediments also leads to the conclusion that the model reproduces the deposition in the north (though at much slower rate), but does not capture transport from west to east.

4.3. Morphodynamic equilibria

Morphodynamical equilibria for semi-enclosed tidal shelf seas have not been found for the configuration and physical mechanisms considered here, because of the persistent export of sediment to the deeper northern basin. This trend will only stop when the deepening has reduced the flow velocities until a negligible amount of sediment is moving. The absence of a morphodynamic equilibrium may be caused by the limited number of physical mechanisms in the model (i.e., local bed-load advection of sand by tidal currents). Disregarding the diffusion, equilibrium can only be obtained when the transports involving the residual current and the tidal asymmetry are equal and of opposite direction. Such conditions occur only locally, however. Additional physical processes are required, which may initially contribute only little, but may eventually allow an equilibrium. The balance between the various terms may be a function of space.

Such additional processes are bed-slope terms and diffusion of suspended sediment (and possibly settling lag). Also, velocity veering in the vertical

by earth rotation (Shapiro et al., 2000; 2004) may be important, because it would affect the direction of the various transport components. Moreover, a threshold of motion could limit erosion. Bed-slope terms act at a smaller spatial scale than resolved here, and are important where bed forms such as tidal sandbanks are present. Tidal sandbanks may play a role in sand budgets at the scale of a field of sandbanks by changing the transport paths into circulation around the banks, as is often observed (e.g., Collins et al., 1995). If this diversion results in reduced or even negligible net sediment transport across a field of sand banks, they may well be essential elements in facilitating a large(r)-scale morphodynamic equilibrium, by allowing for local equilibrium. The dynamic interaction of sand banks with the basin-scale morphodynamic evolution is an interesting topic for further research, but would require a model resolution in the order of 100 m. Diffusion of suspended sediment would transport sediment from shallow areas with high flow velocities to deeper areas. This process would limit seabed topography and export sediment to the northern basin. Hence, it resembles the diffusion term used in the model. It could establish local equilibria. In reality, also non-tidal transport processes such as wind waves, wind-driven currents and possibly density-driven currents will contribute. Waves will enhance the tidal transports dependent on water depth, adding a diffusive tendency that would reduce sea-bed topography. In addition, gradients in the wave field would alter the convergence/divergence of the sediment transports. Dominant southwesterly winds (as exist in western Europe) would increase wave height to the northeast. This might reduce the elevation of the northern shoal and increase the sand export. Climatically averaged wind-induced currents would cause a residual current depending on the bathymetry: with wind direction in shallow areas and in different directions in deeper areas as prescribed by mass conservation (Furnes, 1980). A resulting circulation cell would export sediment and might induce a cross-basin transport component. Transports by wind-induced currents are also enhanced by wind waves.

Considering these contributions, temporary, local morphodynamic equilibria within the southern basin are possible. A process counteracting the export of sediment, however, was not found. Thus, an equilibrium on the scale of the southern basin probably does not exist. Instead, the typical structure of the current amphidromic systems of M_2 and M_4, as dictated by their wavelengths, causes systematic export of sediment towards deeper water, which is aided by the structure of the tidal residual current field. This result implies that fossil shallow sandy shelf deposits, reflecting high-energy tidal sediment transport (e.g., Swift et al., 1991) typically reflect periods of sea-level change, because then water depths of several tens of metres have not persisted long enough to export the high-energy sandy deposits to adjacent deeper basins.

Acknowledgements

The research was funded by the Netherlands Council for Earth and Life Sciences (ALW), with financial aid of the Organisation for Scientific Research (NWO) (NWO-Grant 811.33.005). The authors are very grateful to Jan Backhaus for making the HAMSOM model available. Poppe de Boer and Job Dronkers are thanked for their interest and guidance and for their critical comments on the manuscript. The authors also thank Taco Mulder for carrying out early runs with a different model.

Appendix A. Implementation of the Lax–Wendroff scheme for bed-level change on an Arakawa-C grid

The implementation of Eq. (9) in two dimensions is analogous to the 1D case (Lax and Wendroff, 1960), where intermediate bed levels are computed at an intermediate time level using central differences in space, and final bed levels are computed using information from the intermediate time level, and central differences in space and time.

The numerical implementation of the Lax–Wendroff scheme in two dimensions is as follows:

Step 1: Instantaneous water depths in u- and v-points are computed with

$$h^k_{i+\frac{1}{2},j} = \tfrac{1}{2}(h^k_{i,j} + h^k_{i+1,j}),$$
$$h^k_{i,j+\frac{1}{2}} = \tfrac{1}{2}(h^k_{i,j} + h^k_{i,j+1}). \quad (A.1)$$

Water depths in cell corners follow from

$$h^k_{i+\frac{1}{2},j+\frac{1}{2}} = \tfrac{1}{4}(h^k_{i,j} + h^k_{i+1,j} + h^k_{i,j+1} + h^k_{i+1,j+1}). \quad (A.2)$$

Using Eq. (A.1), velocities in cell centres are computed using flux interpolation

$$u^k_{i,j} = \frac{(uh)^k_{i-\frac{1}{2},j} + (uh)^k_{i+\frac{1}{2},j}}{2h^k_{i,j}},$$
$$v^k_{i,j} = \frac{(vh)^k_{i,j-\frac{1}{2}} + (vh)^k_{i,j+\frac{1}{2}}}{2h^k_{i,j}}, \quad (A.3)$$

and in the cell corners, using Eqs. (A.1) and (A.2), by

$$u^k_{i+\frac{1}{2},j+\frac{1}{2}} = \frac{(uh)^k_{i+\frac{1}{2},j} + (uh)^k_{i+\frac{1}{2},j+1}}{2h^k_{i+\frac{1}{2},j+\frac{1}{2}}},$$
$$v^k_{i+\frac{1}{2},j+\frac{1}{2}} = \frac{(vh)^k_{i,j+\frac{1}{2}} + (vh)^k_{i+1,j+\frac{1}{2}}}{2h^k_{i+\frac{1}{2},j+\frac{1}{2}}}. \quad (A.4)$$

This flux interpolation is essential for the stable operation of the code.

Bed-level slopes in the cell centres are

$$s^k_{x,i,j} = \frac{Z^k_{i+1,j} - Z^k_{i-1,j}}{2\Delta x},$$
$$s^k_{y,i,j} = \frac{Z^k_{i,j+1} - Z^k_{i,j-1}}{2\Delta y}, \quad (A.5)$$

where Δx and Δy are the grid distances. Throughout this paper, $\Delta x = \Delta y$. Also, in the cell corners

$$s^k_{x,i+\frac{1}{2},j+\frac{1}{2}} = \frac{1}{2}\left(\frac{Z^k_{i+1,j} - Z^k_{i,j}}{\Delta x} + \frac{Z^k_{i+1,j+1} - Z^k_{i,j+1}}{\Delta x}\right),$$
$$s^k_{y,i+\frac{1}{2},j+\frac{1}{2}} = \frac{1}{2}\left(\frac{Z^k_{i,j+1} - Z^k_{i,j}}{\Delta y} + \frac{Z^k_{i+1,j+1} - Z^k_{i+1,j}}{\Delta y}\right). \quad (A.6)$$

Sediment transports in the cell centres $q^k_{x,i,j}$ and $q^k_{y,i,j}$ then follow from inserting Eqs. (A.3) and (A.5) into Eq. (4). In the cell corners, sediment transports $q^k_{x,i+\frac{1}{2},j+\frac{1}{2}}$ and $q^k_{y,i+\frac{1}{2},j+\frac{1}{2}}$ are obtained by inserting Eqs. (A.4) and (A.6) into Eq. (4).

Bed levels at $k+\frac{1}{2}$ in u-points are then computed from

$$Z^{k+\frac{1}{2}}_{i+\frac{1}{2},j} = Z^k_{i+\frac{1}{2},j} - \frac{\Delta t}{2}\left[\left(\left\langle q^k_{x,i+1,j}\right\rangle - \left\langle q^k_{x,i,j}\right\rangle\right)\Delta y + \left(\left\langle q^k_{y,i+\frac{1}{2},j+\frac{1}{2}}\right\rangle - \left\langle q^k_{y,i+\frac{1}{2},j-\frac{1}{2}}\right\rangle\right)\Delta x\right] / [(1-p)\Delta x \Delta y] \quad (A.7)$$

where Δt is the morphodynamical time step and $\langle ... \rangle$ denotes averaging over the tide. Similarly, for v-points

$$Z^{k+\frac{1}{2}}_{i,j+\frac{1}{2}} = Z^k_{i,j+\frac{1}{2}} - \frac{\Delta t}{2}\left[\left(\left\langle q^k_{x,i+\frac{1}{2},j+\frac{1}{2}}\right\rangle - \left\langle q^k_{x,i-\frac{1}{2},j+\frac{1}{2}}\right\rangle\right)\Delta y + \left(\left\langle q^k_{y,i,j+1}\right\rangle - \left\langle q^k_{y,i,j}\right\rangle\right)\Delta x\right] / [(1-p)\Delta x \Delta y]. \quad (A.8)$$

Step 2: Velocities at $k+\frac{1}{2}$ in u-points are computed using continuity correction (e.g., Cayocca, 2001)

$$u^{k+\frac{1}{2}}_{i+\frac{1}{2},j} = \frac{(hu)^k_{i+\frac{1}{2},j}}{\zeta^k_{i+\frac{1}{2},j} - Z^{k+\frac{1}{2}}_{i+\frac{1}{2},j}},$$
$$v^{k+\frac{1}{2}}_{i+\frac{1}{2},j} = \frac{(hv)^k_{i,j+\frac{1}{2}} + (hv)^k_{i+1,j+\frac{1}{2}} + (hv)^k_{i,j-\frac{1}{2}} + (hv)^k_{i+1,j-\frac{1}{2}}}{4(\zeta^k_{i+\frac{1}{2},j} - Z^{k+\frac{1}{2}}_{i+\frac{1}{2},j})} \quad (A.9)$$

and in v-points

$$u^{k+\frac{1}{2}}_{i,j+\frac{1}{2}} = \frac{(hu)^k_{i+\frac{1}{2},j} + (hu)^k_{i-\frac{1}{2},j} + (hu)^k_{i+\frac{1}{2},j+1} + (hu)^k_{i-\frac{1}{2},j+1}}{4(\zeta^k_{i,j+\frac{1}{2}} - Z^{k+\frac{1}{2}}_{i,j+\frac{1}{2}})},$$

$$v^{k+\frac{1}{2}}_{i,j+\frac{1}{2}} = \frac{(hv)^k_{i,j+\frac{1}{2}}}{\zeta^k_{i,j+\frac{1}{2}} - Z^{k+\frac{1}{2}}_{i,j+\frac{1}{2}}}, \tag{A.10}$$

where water levels were interpolated in analogy to Eq. (A.1).

Bed slopes in u-points are given by

$$s^{k+\frac{1}{2}}_{x,i+\frac{1}{2},j} = \frac{Z^k_{i+1,j} - Z^k_{i,j}}{\Delta x} \tag{A.11}$$

and in v-points

$$s^{k+\frac{1}{2}}_{y,i,j+\frac{1}{2}} = \frac{Z^k_{i,j+1} - Z^k_{i,j}}{\Delta y}, \tag{A.12}$$

where bed slopes are assumed not to change significantly during half a morphodynamic time step. Sediment transports in the x-direction in u-points $q^{k+\frac{1}{2}}_{x,i+\frac{1}{2},j}$ then follow by substituting Eq. (A.9) and (A.11) into Eq. (4), and sediment transports in the y-direction in v-points $q^{k+\frac{1}{2}}_{y,i,j+\frac{1}{2}}$ by inserting Eq. (A.10) and (A.12) into Eq. (4). New bed levels at $k+1$ in z-points are then given by

$$\begin{aligned} Z^{k+1}_{i,j} = Z^k_{i,j} &- \Delta t \left[\left(\left\langle q^{k+\frac{1}{2}}_{x,i+\frac{1}{2},j} \right\rangle - \left\langle q^{k+\frac{1}{2}}_{x,i-\frac{1}{2},j} \right\rangle \right) \Delta y \right. \\ &\left. + \left(\left\langle q^{k+\frac{1}{2}}_{y,i,j+\frac{1}{2}} \right\rangle - \left\langle q^{k+\frac{1}{2}}_{y,i,j-\frac{1}{2}} \right\rangle \right) \Delta x \right] \\ &/[(1-p)\Delta x \Delta y]. \end{aligned} \tag{A.13}$$

At closed boundaries, zero normal velocities and full slip hydrodynamical conditions were assumed. At open boundaries, Von Neumann conditions were used, i.e., derivatives of the sediment transport perpendicular to the boundary are zero. Cross-boundary bed slopes at all boundaries in the velocity and corner points were set to zero. Bed slopes in the cell centres (water-level/bed-level points) of points adjacent to the boundary were computed from the bed levels of the first two cell centres near the boundary (i.e., first-order analogue of Eq. (A.5)).

Appendix B. Stability and accuracy of the Lax–Wendroff scheme

This appendix presents a relation to approximate the grid size below which the scheme can be applied without artificial stabilisation methods.

The truncation error can be expressed in first approximation in analogy to the linear wave equation:

$$\delta Z \approx \frac{Au^3\Delta x^2}{-2Z(1-p)}(CFL^2 - 1)\frac{\partial^3 Z}{\partial x^3}, \tag{B.1}$$

assuming $\zeta = 0$, $Q = const.$, $u = -Q/Z > 0$, $q = Au^3$, and with $CFL \approx [-3Au^3/2Z(1-p)]\Delta t/\Delta x$.

At the onset of shock waves, the third derivative of the bed level is locally very large, and the truncation error (B.1) will dominate the model solution. For sufficiently small grid sizes, however, the diffusion term resulting from the natural slope term can obtain even larger values, thus ensuring an acceptable solution. In that case, the model can run without artificial correctors. The argumentation below is specific for the present model.

Using the diffusion term resulting from inserting Eq. (4) in Eq. (9), while assuming again that $u = -Q/Z$, and using the truncation error (B.1), the criterion to prevent shock waves becomes

$$\left| \frac{Au^3}{(1-p)\tan\phi_i} \left[\frac{3}{Z} \left(\frac{\partial Z}{\partial x} \right)^2 + \frac{\partial^2 Z}{\partial x^2} \right] \right| > \left| \frac{Au^3\Delta x^2}{-2Z(1-p)}(CFL^2 - 1)\frac{\partial^3 Z}{\partial x^3} \right|. \tag{B.2}$$

Thus, shock waves may be prevented by choosing the grid distance Δx small enough. Practical experience with the test problem of De Vriend (1987) showed that the criterion is satisfied for uni-directional flow when

$$\Delta x < O(-Z). \tag{B.3}$$

For tidal situations, the diffusion term is related directly to the amplitude of the dominant tidal constituent u_2. The truncation error is related to

the tide-averaged sediment transport: $u^3 \approx u_2^2 u_0$, where u_0 in this case represents the combined influence of a residual current and tidal asymmetry. Typically, $u_2 \approx 10u_0$. Thus, for tidal conditions,

$$\Delta x < 10\ O(-Z). \quad \text{(B.4)}$$

References

Arakawa, A., Lamb, V.R., 1977. Computational design of the basic dynamic processes of the UCLA general circulation model. Methods of Computational Physics 16, 173–263.

Backhaus, J.O., 1983. A semi-implicit scheme for the shallow water equations for application to shelf sea modelling. Continental Shelf Research 2, 243–254.

Backhaus, J.O., 1985. A three-dimensional model for the simulation of shelf sea dynamics. Deutsche Hydrografische Zeitschrift 38, 165–187.

Bagnold, R.A., 1963. Mechanics of marine sedimentation. In: Hill, M.N. (Ed.), The Sea: Ideas and Observations, Vol. 3. Wiley-Interscience, New York, pp. 507–528.

Bailard, J.A., 1981. An energetics total load sediment transport model for a plane sloping beach. Journal of Geophysical Research C (Oceans) 86, 10938–10954.

Balson, P.S., 1988. Offshore Geology, East Anglia, Sheet 52°N–00°E, Including the Wash (part of 53°N–00°E) Sea Bed Sediments. British Geological Survey, Natural Environmental Research Council, Ordnance Survey, Southampton, England, UK.

Balson, P.S., D'Olier, B., 1990. Offshore Geology, Thames Estuary, Sheet 51°N–00°E, Sea Bed Sediments and Quaternary Geology. British Geological Survey, Natural Environmental Research Council, Ordnance Survey, Southampton, England, UK.

Balson, P.S., Laban, C., Schüttenhelm, R.T.E., Paepe, R., Baeteman, C., 1991. Offshore Geology, Ostend, Sheet 51°N–02°E, Sea Bed Sediments and Holocene Geology. British Geological Survey, Natural Environmental Research Council, Ordnance Survey, Southampton, England, UK.

Banner, F.T., 1979. Sediments of the north-western European shelf. In: Banner, F.T., Collins, M.B., Massie, K.S. (Eds.), The North-West European Shelf Seas: The Sea Bed and The Sea in Motion, Part I. Geology and Sedimentology. Elsevier Oceanography Series 24A, Elsevier, New York, pp. 271–300.

Beets, D.J., Van der Spek, A.J.F., 2000. The Holocene evolution of the barrier and back-barrier basins of Belgium and the Netherlands as a function of late Weichselian morphology, relative sea-level rise and sediment supply. Geologie en Mijnbouw/Netherlands Journal of Geosciences 79, 3–16.

Cameron, T.D.J., Laban, C., Schüttenhelm, R.T.E., 1984a. Offshore Geology, Flemish Bight, Sheet 52°N–02°E, Sea Bed Sediments and Holocene Geology. British Geological Survey, Natural Environmental Research Council, Ordnance Survey, Southampton, England, UK.

Cameron, T.D.J., Laban, C., Schüttenhelm, R.T.E., 1984b. Offshore Geology, Flemish Bight, Sheet 52°N–02°E, Quaternary Geology. British Geological Survey, Natural Environmental Research Council, Ordnance Survey, Southampton, England, UK.

Cameron, T.D.J., Laban, C., Schüttenhelm, R.T.E., 1986. Offshore Geology, Indefatigable, Sheet 53°N–02°E, Quaternary Geology. British Geological Survey, Natural Environmental Research Council, Ordnance Survey, Southampton, England, UK.

Caston, V.N.D., 1979. The Quaternary sediments of the North Sea. In: Banner, F.T., Collins, M.B., Massie, K.S. (Eds.), The North-West European Shelf Seas: The Sea Bed and the Sea in Motion, Part I. Geology and Sedimentology. Elsevier Oceanography Series 24A, Elsevier, New York, pp. 195–267.

Cayocca, F., 2001. Long-term morphodynamical modeling of a tidal inlet: the Arcachon Basin, France. Coastal Engineering 42, 115–142.

Collins, M.B., Shimwell, S.J., Gao, S., Powell, H., Hewitson, C., Taylor, J.A., 1995. Water and sediment movement in the vicinity of linear sandbanks: the Norfolk Banks, southern North Sea. Marine Geology 123, 125–142.

Davies, A.M., Kwong, S.C.M., 2000. Tidal energy fluxes and dissipation on the European continental shelf. Journal of Geophysical Research C (Oceans) 105, 21969–21989.

De Ruijter, W.P.M., van der Giessen, A., Groenendijk, F.C., 1992. Current and density structure in the Netherlands coastal zone. In: Prandle, D. (Ed.), Dynamics and exchanges in Estuaries and the Coastal Zone, Coastal and Estuarine Studies, Vol. 40. AGU, Washington, DC, pp. 529–550.

De Vriend, H.J., 1987. Analysis of horizontally two-dimensional morphological evolutions in shallow water. Journal of Geophysical Research C (Oceans) 92, 3877–3893.

Dyer, K.R., Huntley, D.A., 1999. The origin, classification and modelling of sandbanks and sand ridges. Continental Shelf Research 19, 1285–1330.

Flather, R.A., 1987. Estimates of extreme conditions of tide and surge using a numerical model of the North-west European Continental Shelf. Estuarine, Coastal and Shelf Science 24, 69–93.

Furnes, G.K., 1980. Wind effects in the North Sea. Journal of Physical Oceanography 10, 978–984.

Gerritsen, H., Berentsen, C.W.J., 1998. A modelling study of tidally induced equilibrium sand balances in the North Sea during the Holocene. Continental Shelf Research 18, 151–200.

Gill, A.E., 1982. Atmosphere–Ocean Dynamics. International Geophysics Series 30. Academic Press, San Diego, 662pp.

Harrison, D.J., Laban, C., Schüttenhelm, R.T.E., 1987. Offshore Geology, Indefatigable, Sheet 53°N–02°E, Sea Bed Sediments and Holocene Geology. British Geological Survey, Natural Environmental Research Council, Ordnance Survey, Southampton, England, UK.

Hulscher, S.J.M.H., de Swart, H.E., de Vriend, H.J., 1993. The generation of offshore tidal sand banks and sand waves. Continental Shelf Research 13, 1183–1204.

Huntley, D.A., Nicholls, R.J., Liu, C., Dyer, K.R., 1994. Measurements of the semi-diurnal drag coefficient over sand waves. Continental Shelf Research 14, 437–456.

Jelgersma, S., Oele, E., Wiggers, A.J., 1979. Depositional history and coastal development in the Netherlands and the adjacent North Sea since the Eemian. In: Oele, E., Schüttenhelm, R.T.E., Wiggers, A.J. (Eds.), The Quaternary History of the North Sea. Acta Universitatis Upsaliensis, Almqvist and Wiksell International, Stockholm, pp. 115–142.

Johnson, M.A., Kenyon, N.H., Stride, A.H., 1982. Sand transport. In: Stride, A.H. (Ed.), Offshore Tidal Sands: Processes and Deposits. Chapman & Hall, New York, pp. 58–94.

Kiden, P., Denys, L., Johnston, P., 2002. Late Quaternary sea-level change and isostatic and tectonic land movements along the Belgian–Dutch North Sea coast: geological data and model results. Journal of Quaternary Science 17, 535–546.

Lambeck, K., 1995. Late Devensian and Holocene shorelines of the British Isles and North Sea from models of glacio–hydro-isostatic rebound. Journal of the Royal Society, London 152, 437–448.

Lanzoni, S., Seminara, G., 2002. Long-term evolution and morphodynamic equilibrium of tidal channels. Journal of Geophysical Research C (Oceans) 107, 11–20.

Lax, P., Wendroff, B., 1960. Systems of conservation laws. Communications on Pure and Applied Mathematics 13, 217–237.

Lee, J.C., Jung, K.T., 1999. Application of eddy viscosity closure models for the M_2 tide and tidal currents in the Yellow Sea and the East China Sea. Continental Shelf Research 19, 445–475.

Nairn, R.B., Southgate, H.N., 1993. Deterministic profile modelling of nearshore processes. Part 2. Sediment transport and beach profile development. Coastal Engineering 19, 57–96.

Oele, E., Schüttenhelm, R.T.E., 1979. Development of the North sea after the Saalian glaciation. In: Oele, E., Schüttenhelm, R.T.E., Wiggers, A.J. (Eds.), The Quaternary History of the North Sea. Acta Universitatis Upsaliensis, Uppsala, pp. 191–231.

Otto, L., Zimmerman, J.T.F., Furnes, G.K., Mork, M., Saetre, R., Becker, G., 1990. Review of the physical oceanography of the North Sea. Netherlands Journal of Sea Research 26, 161–238.

Parker, B.B., 1991. Tidal Hydrodynamics. Wiley, New York, 883pp.

Pingree, R.D., Griffiths, D.K., 1979. Sand transport paths around the British Isles resulting from M_2 and M_4 tidal interactions. Journal of the Marine Biological Association of the UK 59, 497–513.

Pingree, R.D., Griffiths, D.K., Maddock, L., 1984. Quarter diurnal shelf resonances and tidal bed stress in the English Channel. Continental Shelf Research 3, 267–289.

Prandle, D., 1978. Residual flows in the southern North Sea. Proceedings of the Royal Society of London Series A 359, 189–228.

Prandle, D., 1980. Co-tidal charts for the southern North Sea. Deutsche Hydrographische Zeitschrift 33, 68–81.

Prandle, D., Loch, S.G., Player, R., 1993. Tidal flow through the straits of Dover. Journal of Physical Oceanography 23, 23–37.

Ranasinghe, R., Pattiaratchi, C., Masselink, G., 1999. A morphodynamical model to simulate the seasonal closure of tidal inlets. Coastal Engineering 37, 1–36.

Rienecker, M.M., Teubner, M.D., 1980. A note on frictional effects in Taylor's problem. Journal of Marine Research 38, 183–191.

Schuttelaars, H.M., De Swart, H.E., 2000. Multiple morphodynamical equilibria in tidal embayments. Journal of Geophysical Research C (Oceans) 105, 24105–24118.

Schramkowski, G.P., Schuttelaars, H.M., De Swart, H.E., 2002. The effect of geometry and bottom friction on local bed forms in a tidal embayment. Continental Shelf Research 22, 1821–1833.

Seminara, G., Tubino, M., 2001. Sand bars in tidal channels. Part 1: free bars. Journal of Fluid Mechanics 440, 49–74.

Shapiro, G.I., Akivis, T.M., Pykhov, N.V., Antsyferov, S.M., 2000. Transport of fine sediment with mesoscale currents in the shelf-slope zone of the sea. Oceanology 40, 305–311.

Shapiro, G.I., Van der Molen, J., De Swart, H.E., 2004. The effect of velocity veering on sand transport on a shallow sea. Ocean Dynamics, in press.

Soulsby, R., 1997. Dynamics of Marine Sands. Thomas Telford, London, 249pp.

Stelling, G.S., Duinmeijer, S.P.A., 2003. A staggered conservative scheme for every Froude number in rapidly varied shallow water flows. International Journal for Numerical Methods in Fluids 43(12), 1329–1354.

Swift, D.J.P., Oertel, G.F., Tillman, R.W., 1991. Shelf sand and sandstone bodies: geometry, facies and sequence stratigraphy. In: Special publications International Association of Sedimentologists, Vol. 14. Blackwell, Oxford, pp. 534.

Taylor, G.I., 1920. Tidal oscillations in gulfs and rectangular basins. Proceedings of the London Mathematical Society2 20(2), 148–181.

Van de Kreeke, J., Robaczewska, K., 1993. Tide-induced residual transport of coarse sediment; application to the Ems Estuary. Netherlands Journal of Sea Research 31, 209–220.

Van der Molen, J., 2002. The influence of tides, wind and waves on the net sand transport in the North Sea. Continental Shelf Research 22, 2739–2762.

Van der Molen, J., 2003. Bailard's sediment transport formulation in shelf sea conditions: comparison with observations using a clustering technique. Coastal Engineering 47, 399–412.

Van der Molen, J., De Swart, H.E., 2001. Holocene tidal conditions and tide-induced sand transport in the southern North Sea. Journal of Geophysical Research C (Oceans) 106, 9339–9362.

Van Leeuwen, S.M., De Swart, H.E., 2001. The effect of advective processes on the morphodynamic stability of short tidal embayments. Physics and Chemistry of the Earth B 26, 735–740.

Williams, J.J., Humphery, J.D., Hardcastle, P.J., Wilson, D.J., 1998. Field observations of hydrodynamic conditions and suspended particulate matter in the southern North Sea. Continental Shelf Research 18, 1215–1233.

Xia Zongwan, Carbajal, N., Sündermann, J., 1995. Tidal current amphidromic systems in semi-enclosed basins. Continental Shelf Research 15, 219–240.

Zheng Fang, Anle Ye, Gouhong Fang, 1991. Solutions of tidal motions in a semi-closed rectangular gulf with open boundary condition specified. In: Parker, B.B. (Ed.), Tidal Hydrodynamics, Wiley, New York, pp. 153–168.

Zhu, Y., Chang, R., 2000. Preliminary study of the dynamic origin of the distribution pattern of bottom sediments on the continental shelves of the Bohai Sea, Yellow Sea and East China Sea. Estuarine, Coastal and Shelf Science 51, 663–680.